Covalent states and spin-orbit coupling in electronic and magnetic properties of $Ba_6Y_2Rh_2Ti_2O_{17}$

Jihai Yu,[1] Lin Wu,[1] Di Wang,[1] Qingfang Li,[2,*] Weifeng Zhang,[3] Xiangang Wan,[1,4] and Jian Zhou[5,6,†]

[1]*National Laboratory of Solid State Microstructures and Department of Physics, Nanjing University, Nanjing 210093, China*

[2]*Department of Physics, Nanjing University of Information Science and Technology, Nanjing 210044, China*

[3]*Key Laboratory for Quantum Physical Sciences, Henan University, Kaifeng 475004, China*

[4]*Collaborative Innovation Center of Advanced Microstructures, Nanjing University, Nanjing 210093, China*

[5]*National Laboratory of Solid State Microstructures and Department of Materials Science and Engineering, Nanjing University, Nanjing 210093, China*

[6]*Jiangsu Key Laboratory of Artificial Functional Materials, Nanjing University, Nanjing 210093, China*

(Received 31 May 2021; revised 27 July 2021; accepted 3 August 2021; published 16 August 2021)

In 4*d* and 5*d* transition metal compounds, novel properties usually arise from the interplay of electron correlation and spin-orbit interaction based on isolated single-site physics. However, there are also a large number of compounds where the intersite effect plays an important role. Here, we report the electronic and magnetic properties of a hexagonal perovskite $Ba_6Y_2Rh_2Ti_2O_{17}$, which is featured with widely spaced Rh_2O_9 spin dimers. Our calculations indicate that $Ba_6Y_2Rh_2Ti_2O_{17}$ is a semiconductor with a small band gap of 0.2 eV, which is consistent with the experimental value of 0.16 eV. In particular, the band gap of $Ba_6Y_2Rh_2Ti_2O_{17}$ is not due to the $J_{\text{eff}} = 1/2$ state from isolated single site but due to the joint effect of covalent states and spin-orbit coupling formed by Rh's t_{2g} orbitals inside the Rh_2O_9 dimers. Furthermore, we find a giant magnetic anisotropy energy (MAE) of about 20 meV/Rh in $Ba_6Y_2Rh_2Ti_2O_{17}$ with the easy axis being the *c* axis. Model calculations show that the giant MAE is mainly due to first-order perturbation on the doubly degenerate antibonding states of e_g^{π} orbitals. Our work not only reveals the interesting electronic and magnetic properties of $Ba_6Y_2Rh_2Ti_2O_{17}$ but also could stimulate more studies on the materials with 4*d* and 5*d* spin dimers.

DOI: 10.1103/PhysRevB.104.075123

I. INTRODUCTION

The rhodium-based compounds have been widely investigated over the past decades because of their unusual electronic and magnetic properties. For example, the layered material Sr_2RhO_4 hosts the paramagnetic metallic state [1–3] while Sr_4RhO_6 is the spin-orbit driven magnetic insulator with $J_{\text{eff}} = 1/2$ character [4]. Both materials have quadrivalent rhodium cations (Rh^{4+}) coordinated by six divalent oxygen anions, forming RhO_6 octahedra. Therefore, their low-energy electronic structures are dominated by the t_{2g} bands filled by five *d* electrons under large crystal field splitting. The RhO_6 octahedra in Sr_2RhO_4 are corner sharing and have larger distortion but in Sr_4RhO_6 they are spatially separated and almost maintain perfect cubic structures. These different features result in large bandwidth in Sr_2RhO_4 and strong single-site effect in Sr_4RhO_6, which makes them hold different ground states. Besides, similar octahedra occur in $CaRhO_3$ which is crystallized in a perovskite structure [5] and can transform into a postperovskite structure by subsequent annealing [6]. The two bulk structures show paramagnetic metallic state and antiferromagnetic (AFM) state, respectively. However, the isostructural $SrRhO_3$ films have the evidence to demonstrate magnetism which differs from the paramagnetic metallic ground state that governs in the bulk samples. This is also strongly related to rotations of RhO_6 octahedra [7,8]. Moreover, layered material $K_{0.5}RhO_2$ with edge-sharing RhO_6 octahedra is predicted to hold noncoplanar AFM configuration and a quantum topological Hall insulating phase [9].

In all materials mentioned above, there exist RhO_6 octahedra with different connections which are very crucial to their ground states. Recently, a hexagonal material $Ba_6Y_2Rh_2Ti_2O_{17}$ containing RhO_6 octahedral dimers has been synthesized [10]. The electric transport and optical experiments show that the material is a semiconductor with a band gap of 0.16 eV at low temperatures. However, a large temperature-linear term in the specific heat is observed which provides evidence to support the material $Ba_6Y_2Rh_2Ti_2O_{17}$ as a spin liquid candidate [10]. Besides, the Curie-Weiss fitting from the high-temperature magnetic susceptibility of $Ba_6Y_2Rh_2Ti_2O_{17}$ implies the weak AFM interactions with an effective moment of $\mu_{\text{eff}} = 1.52\mu_B$/dimer. This is much smaller than the expected value ($\mu_{\text{eff}} = 3.46\mu_B$/dimer) from the spin moment of Rh^{4+}. The possible mechanisms such as charge order and joint effect of spin-orbit coupling (SOC) and singlet molecular orbitals of suppression on magnetic moments in the similar dimer structures were proposed [11,12].

The most important structural feature of $Ba_6Y_2Rh_2Ti_2O_{17}$ is that a pair of RhO_6 octahedra are combined through face-sharing connection, forming a dimer structure [10,13]. The valence of Rh in $Ba_6Y_2Rh_2Ti_2O_{17}$ would be +4 with five electrons in its 4*d* shell since Ba, Y, Ti,

*qingfangli@nuist.edu.cn
†zhoujian@nju.edu.cn

and O are +2, +3, +4, and −2, respectively. However, in contrast to the single-site physics ($J_{\text{eff}} = 1/2$ state), here we deal with a strongly coupled pair of Rh ions. The intersite electron hopping would play an important role, similar to its intra-atomic parameters, such as Hund's exchange coupling (J_H), SOC strength (λ), and intra-atomic Hubbard repulsion (U). Indeed, in going from 3*d* to 4*d* and 5*d* orbitals, the Hubbard U decreases, from about 5 eV for 3*d* orbitals to 2–3 eV for 4*d* orbitals, and then to 1–2 eV for 5*d* orbitals. Similarly, the Hund's coupling J_H also gradually decreases, from 0.7–0.9 eV for 3*d* orbitals to 0.5–0.6 for 4*d* orbitals, and then to about 0.5 eV for 5*d* orbitals [14]. At the same time, with the size of *d* orbitals increasing in this series the *p*-*d* and *d*-*d* hoppings can easily reach 1–1.5 eV for 4*d*-5*d* materials [15–17]. In this situation, there may occur strong modification of the behavior expected for isolated 4*d* (e.g.,Rh) ions. $Ba_6Y_2Rh_2Ti_2O_{17}$ may be a good example in which one can investigate the relative importance of single-site versus intersite effects.

In this paper, we systematically investigate the electronic and magnetic properties of $Ba_6Y_2Rh_2Ti_2O_{17}$ by using the first-principles calculations. We find that there exists a strong covalent state in this material. Based on the orbital energy level formed by the intersite effect, Hund's coupling is taken into consideration and the bands are split into spin-up and spin-down channels. The SOC plays an important role in opening the band gap of $Ba_6Y_2Rh_2Ti_2O_{17}$. The covalent states and SOC introduce interstitial moments and orbital moments, respectively. In addition, the SOC introduces a giant single-ion magnetic anisotropy energy (MAE) due to the first-order perturbation on the doubly degenerate antibonding states of e_g^{π} orbitals around the Fermi level.

II. COMPUTATIONAL DETAILS

The electronic band structures and density of states calculations of $Ba_6Y_2Rh_2Ti_2O_{17}$ have been carried out by using the full potential linearized augmented plane wave method as implemented in the WIEN2K package [18]. We use the local spin density approximation (LSDA) exchange-correlation functional in our calculations since it is widely used for various transition metal compounds [19–21]. A 6×6 × 2 *k*-point mesh is used for the Brillouin zone integral. The SOC effect is included by using the second-order variational procedure since it plays an important role in materials with heavy elements [22–24]. We utilize the LSDA + U scheme to take into account the effect of Coulomb repulsion in 4*d* orbitals of Rh ions [25] and vary the parameter U between 1.0 and 4.0 eV. The radii of muffin-tin spheres are 2.28, 1.93, 2.18, 1.57, and 1.42 Bohr for Ba, Y, Rh, Ti, and O ions, respectively. The size of the bases is controlled by the condition of $R_{\text{mt}}K_{\text{max}} = 7$, where R_{mt} is the smallest muffin-tin sphere radius in the unit cell and K_{max} is the largest reciprocal lattice vector used in the plane-wave expansion. Based on the experimental lattice constants, we optimize all independent internal atomic coordinates and confirmed that the structural parameters are in good agreement with the experimental results (see Table I). Thus we perform all calculations based on the experimental structure [10]. In the structural optimization and self-consistent calculations, the convergences of the total energy and the maximum force tolerance are set to be 0.1 mRy and 1.0 mRy/Bohr, respectively. For the magnetic calculations, we consider the ferromagnetic (FM) and AFM configurations for the two Rh ions in the same dimer of $Ba_6Y_2Rh_2Ti_2O_{17}$.

TABLE I. Selective theoretical and experimental bond lengths (Å) and angles (°) of $Ba_6Y_2Rh_2Ti_2O_{17}$.

Bond lengths	This work	Experiment [10]
Rh-Rh	2.571	2.520
Rh-O_1	1.969	2.001
Rh-O_2	2.024	1.965
Angles	This work	Experiment [10]
O_1-Rh-O_1	91.5	91.1
O_2-Rh-O_2	84.0	83.3

III. RESULTS AND DISCUSSION

A. Crystal structure

The material $Ba_6Y_2Rh_2Ti_2O_{17}$ is crystallized in the hexagonal structure (space group $P6_3/mmc$) [10], as shown in Fig. 1(a). It has a large unit cell, with the experimental lattice constants of $a = b = 5.920$ Å and $c = 29.497$ Å, which contains two formula units and a total of 58 atoms. These atoms are located at 11 nonequivalent crystallographic sites. The Rh ions are located at the 4*f* position: (1/3, 2/3, 0.7073), each of which is coordinated by six oxygens forming a slightly distorted RhO_6 octahedron. The average length of six Rh-O bonds is 1.98 Å. It is worthwhile to mention that two RhO_6 octahedra are face sharing and form a Rh_2O_9 dimer, as shown in Fig. 1(b). This special connecting mode between the octahedra may result in interesting features of orbital and spin structure, such as strongly AFM quantum magnets [26] and highly symmetric SU(4) spin-orbital model [27]. As shown in Fig. 1(b), the nearest neighboring Rh-Rh distance across the common face is 2.52 Å, which is even smaller than that in rhodium metal (2.69 Å [28]). There are two Rh_2O_9 dimers in

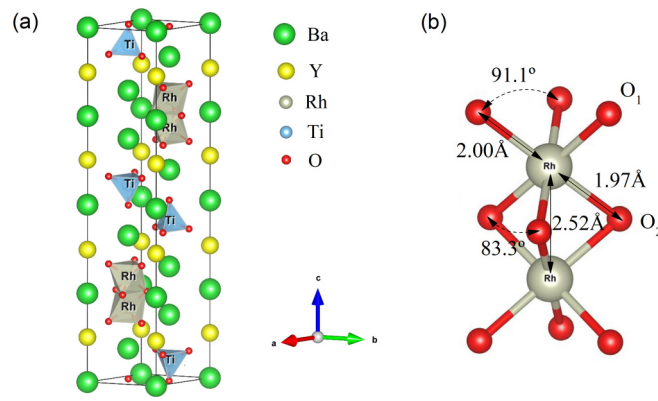

FIG. 1. (a) Hexagonal crystal structure of $Ba_6Y_2Rh_2Ti_2O_{17}$. The green, yellow, grey, blue, and red balls represent the Ba, Y, Rh, Ti, and O ions, respectively. Rh and Ti ions are at the center of RhO_6 octahedron and TiO_4 tetrahedron, respectively. (b) The optimized Rh_2O_9 dimer and its related structural parameters.

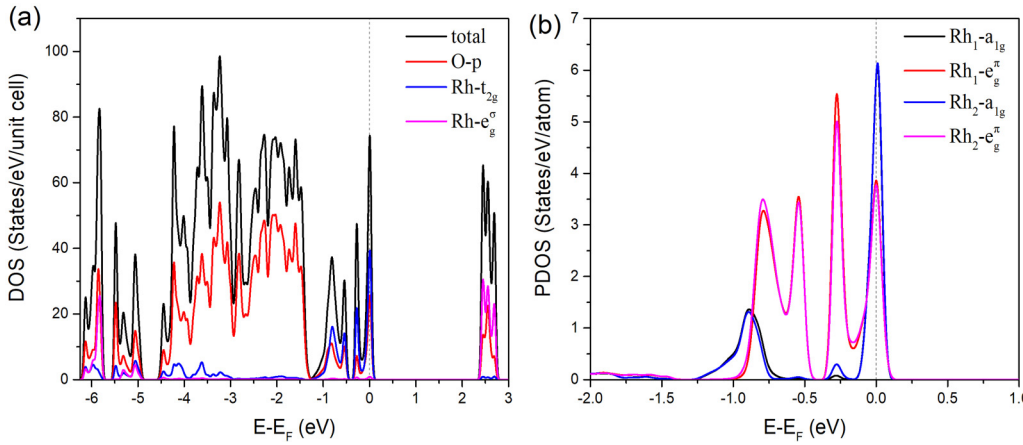

FIG. 2. (a) Total and partial density of states. (b) Partial density of states of Rh projected in the octahedral local coordinate system of $Ba_6Y_2Rh_2Ti_2O_{17}$ based on the nonmagnetic LDA calculation. The Fermi energy is set to zero.

one unit cell belonging to different layers, separated by 14.76 Å along the c axis, while the two dimers in the same plane obey the triangular arrangement, with the distance of 5.94 Å. These remarkable structural features of $Ba_6Y_2Rh_2Ti_2O_{17}$ significantly affect its electronic band structure and magnetic properties.

B. Nonmagnetic calculation and covalent states

To have a basic understanding of the compound $Ba_6Y_2Rh_2Ti_2O_{17}$, we first perform the local density approximation (LDA) calculations. The calculated partial density of states (PDOS) and band structure are given in Figs. 2 and 4(a), respectively. Since the Ba, Y, and Ti atoms are highly ionic, their bands are far away from the Fermi energy, which is mainly located either below −6 eV or above 4 eV (not shown here). The valence bands between −6.0 and −1.5 eV are dominated by O's 2p bands with some contributions of Rh's 4d orbitals due to the p-d hybridization. Hence the chemical valence for O is −2 and the nominal valence of Rh in $Ba_6Y_2Rh_2Ti_2O_{17}$ is +4. So the electronic configuration of the Rh ion is $4d^5$. The density of states (DOS) around the Fermi energy is mainly contributed by Rh's 4d orbitals. Due to the RhO_6 octahedral crystal field, the Rh's 4d orbitals split into the t_{2g} (d_{xy}, d_{yz}, and d_{xz}) and e_g^σ (d_{z^2}, and $d_{x^2-y^2}$) ones. The estimated crystal field splitting energy is about 3 eV and the 12 t_{2g} bands from four Rh ions are mainly located from −1.2 to 0 eV, as shown in Fig. 2(a). The e_g^σ orbitals have larger hybridization with O ions due to their distribution mainly along the Rh-O line. And the t_{2g} DOS between −6 and −3 eV in Fig. 2(a) indicates the distortion of the octahedral crystal field.

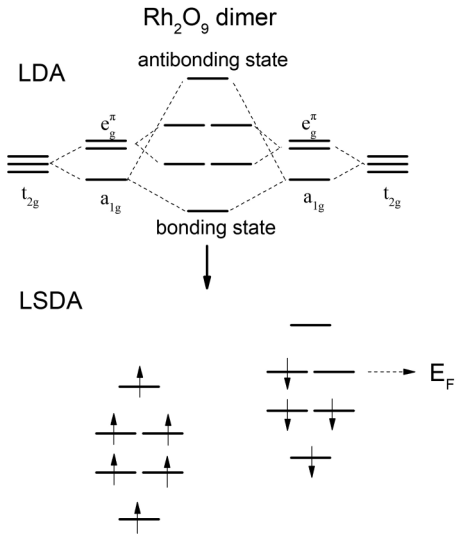

FIG. 3. The schematic picture of orbital occupation around Fermi level.

In 4d and 5d transition metal oxides, t_{2g} bands are usually transformed into $J_{\text{eff}} = 1/2$ states due to large SOC in a single-site environment. However, here the distorted octahedral and dimerized structure result in covalent states as shown in Fig. 2(b). In detail, the t_{2g} bands will further split into nondegenerate a_{1g} orbital $\frac{1}{\sqrt{3}}(d_{xy} + d_{yz} + d_{xz})$ and doubly degenerate e_g^π orbitals $\frac{1}{\sqrt{3}}(d_{xy} + e^{i2\pi/3}d_{yz} + e^{-i2\pi/3}d_{xz})$ and $\frac{1}{\sqrt{3}}(d_{xy} + e^{-i2\pi/3}d_{yz} + e^{i2\pi/3}d_{xz})$ due to the large distortion of the RhO_6 octahedron. And the energy of the a_{1g} orbital is usually slightly lower than that of the e_g^π ones in a dimer structure. As we can see in Fig. 2(b), the PDOS of a_{1g} takes place on both sides of that of e_g^π. This implies that the two face-sharing Rh orbitals will bond with each other, leading to the orbital occupation as shown in Fig. 3. Since the electrons of the a_{1g} orbital are mostly localized along the connecting line between the two Rh cations in one Rh_2O_9 dimer, it leads to larger bonding-antibonding splitting for the a_{1g} orbital than that for the e_g^π orbitals. The energy size of the a_{1g} bonding-antibonding splitting is about 0.9 eV. The LDA calculation produces a metallic state due to partially occupied covalent states formed by Rh's t_{2g} orbitals.

C. Magnetic calculation and spin-orbit coupling

Our nonmagnetic LDA calculation indeed finds a sizable bonding-antibonding splitting. Then we do the spin-polarized calculations to understand the magnetism of

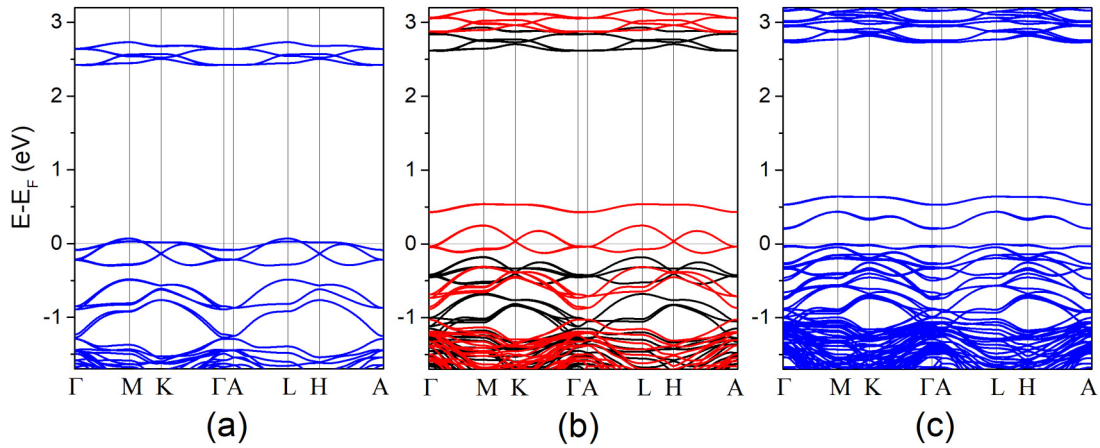

FIG. 4. Band structures of $Ba_6Y_2Rh_2Ti_2O_{17}$ from the (a) LDA, (b) LSDA + U ($U = 2$ eV), and (c) LSDA + SOC + U ($U = 2$ eV) calculations. The Fermi energy is set to zero. The black and red lines in panel (b) represent spin-up and spin-down bands, respectively.

$Ba_6Y_2Rh_2Ti_2O_{17}$. The band structure of FM configuration is shown in Fig. 3(b). As we introduce the Hund's exchange coupling, the degenerate energy level will split into spin-up and spin-down ones, as shown in Fig. 3. There are ten electrons filling in the orbitals of one Rh_2O_9 dimer and the Fermi energy will locate at the e_g^{π} antibonding states between two Rh ions. Since the orbital is half filled, we can expect the metallic solution in the LSDA calculation. It is well known that Hubbard U can easily gap the half-filled band with small bandwidth leading to the metal-insulator transition. However, the LSDA + U calculations give the metallic bands which keep for different U values varying from 1 to 4 eV. The band structure based on the LSDA + U ($U = 2$ eV) calculation is present in Fig. 4(b), which is metallic. Since the reasonable Hubbard U is about 2–3 eV for 4d transition metal [14,29], we believe that the LSDA + U calculations could not open the band gap in $Ba_6Y_2Rh_2Ti_2O_{17}$ and they also give a metallic ground state like the case of LDA.

The strengths of SOC in 4d orbitals are about 0.1–0.3 eV [30], which is one order of magnitude larger than those of the 3d ones. Therefore, SOC usually changes the electronic properties of 4d electron significantly and can play an essential role in the band gap opening. To investigate the effect of SOC in $Ba_6Y_2Rh_2Ti_2O_{17}$, we then calculate the band structure with SOC, which is given in Fig. 4(c). We can see that once we include the SOC, a band gap of about 0.2 eV is opened, which is close to the experimental value of 0.16 eV. We also perform the LSDA + SOC + U ($U = 2$–4 eV) calculations and obtain increasing band gap as shown in Table II. Therefore, SOC is a critical factor in opening the band gap of $Ba_6Y_2Rh_2Ti_2O_{17}$ which could be enhanced gradually by Hubbard U.

We also present the total energy and magnetic properties of $Ba_6Y_2Rh_2Ti_2O_{17}$ by the LSDA + SOC + U calculations in Table II. When $U = 1$ eV, the AFM configuration converges to the FM state, thus we do not list the result. When the Hubbard U is in the range 2–4 eV, the total energy of the FM configuration is always much lower than that of the AFM one, indicating a strong FM coupling between two Rh ions in the same dimer. However, a small negative Curie-Weiss temperature of -2.8 K was found in the experiment, which implies the weak AFM interaction in this material [10]. Considering the strong FM coupling inside the dimer, we believe that the small negative Curie-Weiss temperature in $Ba_6Y_2Rh_2Ti_2O_{17}$ is due to weak AFM interdimers interactions caused by the large distance (about 5.94 Å) and triangular arrangement of Rh_2O_9 dimers.

As shown in Table II, it is found that the spin and orbital moments at each Rh ion are $0.60\mu_B$ and $0.26\mu_B$ respectively, while the interstitial moments from the covalent states are $0.23\mu_B$ from the LSDA + SOC + U ($U = 2$ eV) calculation. The O ions in the Rh_2O_9 dimers also carry a small but nonvanishing moment due to the p-d hybridization with Rh atoms.

D. Magnetic anisotropy energy

Finally, we study the MAE of $Ba_6Y_2Rh_2Ti_2O_{17}$ by performing the LSDA + SOC + U ($U = 2$ eV) calculation with the FM configuration for three different orientations of magnetic moment: along (001), (010), and (100) directions. Our calculations show that (001) is the easy axis while (010) and (100) are the hard axes and share the same total energy. We list the calculated magnetic moments and total energies in Table III. Remarkably, we find that $Ba_6Y_2Rh_2Ti_2O_{17}$ has a giant MAE, which is around 40 meV per Rh_2O_9 dimer (20 meV per Rh atom) with the highly preferential easy axis being the c

TABLE II. Calculated band gap, spin moments (m_{spin}), orbital moments ($m_{orbital}$), interstitial moments ($m_{interstitial}$), total energy difference (ΔE) per Rh_2O_9 dimer in the FM configuration from the LSDA + SOC + U calculations. The spin is along the c axis. The total energy difference (ΔE) is defined as the energy difference between the FM and AFM configurations. The total energy of AFM configuration is set to zero.

LSDA + SOC + U	$U = 2$ eV	$U = 3$ eV	$U = 4$ eV
Gap (eV)	0.20	0.26	0.30
m_{spin} (μ_B)	1.20	1.22	1.24
$m_{orbital}$ (μ_B)	0.52	0.58	0.62
$m_{interstitial}$ (μ_B)	0.23	0.22	0.22
ΔE (meV)	-216	-242	-180

TABLE III. Calculated total energy difference (ΔE), spin moments (m_{spin}), orbital moments (m_{orbital}), interstitial moments ($m_{\text{interstitial}}$) per Rh_2O_9 dimer in the FM configuration from the LSDA + SOC + U ($U = 2$ eV) calculations with different spin directions. The total energy of spin orientation along the (001) direction is set to zero.

Spin directions	ΔE (meV)	m_{spin} (μ_B)	m_{orbital} (μ_B)	$m_{\text{interstitial}}$ (μ_B)
(001)	0	1.20	0.51	0.23
(100)/(010)	40	1.18	0.02	0.22

axis. This MAE is close to the size of the anisotropy energy of other adsorbed or freestanding transition-metal dimers such as Pt-Ir on the defected graphene, Co-Co, and Rh-Rh with MAEs of 30–70 meV [31,32], which may have practical applications at room temperatures.

To understand the origin of MAE, we consider the single-ion anisotropy with orbital energy level and the electronic occupation shown in Fig. 3. The SOC Hamiltonian is [33,34]

$$H_{soc} = \lambda \hat{S}_{z'}\left(\hat{L}_z\cos\theta + \frac{1}{2}\hat{L}_+e^{-i\varphi}\sin\theta + \frac{1}{2}\hat{L}_-e^{i\varphi}\sin\theta\right) + \frac{\lambda}{2}\hat{S}_{+'}\left(-\hat{L}_z\sin\theta - \hat{L}_+e^{-i\varphi}\sin^2\frac{\theta}{2} + \hat{L}_-e^{i\varphi}\cos^2\frac{\theta}{2}\right) + \frac{\lambda}{2}\hat{S}_{-'}\left(-\hat{L}_z\sin\theta + \hat{L}_+e^{-i\varphi}\cos^2\frac{\theta}{2} + \hat{L}_-e^{i\varphi}\sin^2\frac{\theta}{2}\right),$$

where λ is the SOC constant, θ and ϕ are the azimuthal and polar angles of the spin direction with respect to the local coordinate. The (111) direction in local coordinate ($\theta = \arccos\frac{1}{\sqrt{3}}, \phi{=}\frac{\pi}{4}$) is equal to the (001) direction, i.e., the c axis in Fig. 1. As we can see from Fig. 3, the antibonding states of e_g^π orbitals are doubly degenerate with the absence of SOC around the Fermi level. Thus it can be expected that the SOC Hamiltonian has the first-order energy term proportional to λ on MAE from the degenerate perturbation, which is more important than the higher Nth ($N \geqslant 2$) order terms ($\propto \lambda^N$) omitted here. Following the standard degenerate perturbation theory, we consider the SOC Hamiltonian as the perturbation part and obtain its matrix in the e_g^π orbitals subspace:

$$\begin{bmatrix} \langle e_{g1}^\pi, \downarrow | H_{soc} | e_{g1}^\pi, \downarrow\rangle & \langle e_{g1}^\pi, \downarrow | H_{soc} | e_{g2}^\pi, \downarrow\rangle \\ \langle e_{g2}^\pi, \downarrow | H_{soc} | e_{g1}^\pi, \downarrow\rangle & \langle e_{g2}^\pi, \downarrow | H_{soc} | e_{g2}^\pi, \downarrow\rangle \end{bmatrix}.$$

The $|\downarrow\rangle$ represents spin down. The e_{g1}^π and e_{g2}^π orbitals represent $\frac{1}{\sqrt{3}}(d_{xy} + e^{i2\pi/3}d_{yz} + e^{-i2\pi/3}d_{xz})$ and $\frac{1}{\sqrt{3}}(d_{xy} + e^{-i2\pi/3}d_{yz} + e^{i2\pi/3}d_{xz})$, respectively. We diagonalize the matrix and get the energy splitting as $\pm\lambda(\cos\theta + \sin\theta\cos\phi + \sin\theta\sin\phi)/2\sqrt{3}$. Then it is found that the splitting for the spin polarization along the (001) direction is $\pm\frac{\lambda}{2}$, while the antibonding states formed by e_g^π orbitals remain doubly degenerate when the spin polarization is along the (100) and (010) directions. This model analysis is consistent with our band structures from LSDA + SOC + U ($U = 2$ eV) calculation, as shown in Fig. 5. As we can see from Fig. 5(a), the bands made up of two antibonding states in the band structure of the (100) spin direction are close to each other at the vicinity of the Fermi level like LSDA + U calculations. However,

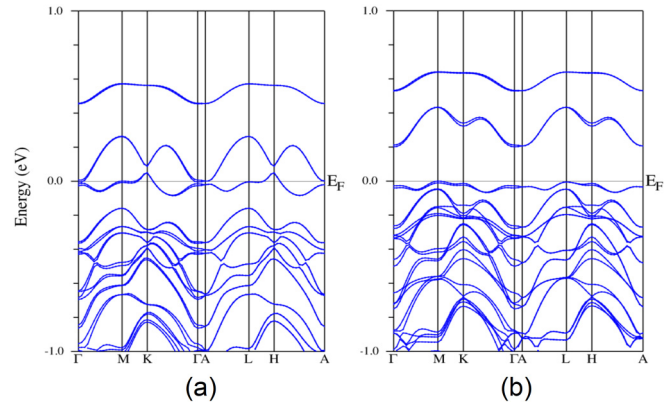

FIG. 5. Band structure of $Ba_6Y_2Rh_2Ti_2O_{17}$ from LSDA + SOC + U ($U = 2$ eV) calculation. Spin orientations along the (a) (100) and (b) (001) direction, respectively. The Fermi energy is set to zero.

they separate when we set the spin direction along (001). One of them is pushed down and becomes fully occupied. This makes the total energy of the (001) direction lower than that of the (100) direction, which mainly contributes to the single-ion anisotropy. The other degenerate orbital energy levels below the Fermi energy are also split but they have no contributions due to being fully occupied. In addition, from the splitting energy result introduced by SOC we can know that not only does the (100) spin direction have zero energy splitting but also all directions perpendicular to the (001) direction, i.e., spin directions lying in the *ab* plane share the same results.

IV. CONCLUSIONS

We perform first-principles calculations on the recent synthesized hexagonal perovskite $Ba_6Y_2Rh_2Ti_2O_{17}$. It is found that there exists a strong interplay of covalent state and SOC in this material. The LSDA + U calculations give a metallic solution for the different U values varying from 1 to 4 eV. When SOC is included, it becomes a semiconductor with a small band gap of 0.2 eV, which is close to the experimental value of 0.16 eV [10]. Although this band gap originates from the SOC, it is not the $J_{\text{eff}} = 1/2$ state from an isolated single site but the covalent states inside the Rh_2O_9 dimers. We also find a giant MAE of 40 meV/dimer (i.e., 20 meV/Rh) in $Ba_6Y_2Rh_2Ti_2O_{17}$ due to the first-order perturbation on the doubly degenerate antibonding states of e_g^π orbitals. Our work demonstrates that the strong intersite coupling may invalidate the single-site picture and lead to more novel properties in the materials with spin dimers.

ACKNOWLEDGMENTS

This work was supported by the National Natural Science Foundation of China (Grants No. 11974163, No. 11890702, No. 51721001, No. 12004170, and No. 11974099), the Natural Science Foundation of Jiangsu Province, China (Grant No. BK20200326), and the Qing Lan Project of Jiangsu Province (Grant No. R2019Q04). The numerical calculations in this paper have been done on the computing facilities in the High Performance Computing Center (HPCC) of Nanjing University.

[1] S. J. Moon, M. W. Kim, K. W. Kim, Y. S. Lee, J.-Y. Kim, J.-H. Park, B. J. Kim, S.-J. Oh, S. Nakatsuji, Y. Maeno, I. Nagai, S. I. Ikeda, G. Cao, and T. W. Noh,Electronic structures of layered perovskite Sr_2MO_4 (M = Ru, Rh, and Ir), Phys. Rev. B **74**, 113104 (2006).

[2] L. J. Sandilands, W. Kyung, S. Y. Kim, J. Son, J. Kwon, T. D. Kang, Y. Yoshida, S. J. Moon, C. Kim, and T. W. Noh, Spin-Orbit Coupling and Interband Transitions in the Optical Conductivity of Sr_2RhO_4, Phys. Rev. Lett. **119**, 267402 (2017).

[3] G. Zhang and E. Pavarini, Optical conductivity, fermi surface, and spin-orbit coupling effects in Sr_2RhO_4, Phys. Rev. B **99**, 125102 (2019).

[4] S. Calder, L. Li, S. Okamoto, Y. Choi, R. Mukherjee, D. Haskel, and D. Mandrus, Spin-orbit driven magnetic insulating state with $J_{\text{eff}} = 1/2$ character in a 4*d* oxide, Phys. Rev. B **92**, 180413(R) (2015).

[5] K. Yamaura and E. Takayama-Muromachi, High-pressure synthesis of the perovskite rhodate $CaRhO_3$, Phys. C (Amsterdam, Neth.) **445**, 54 (2006).

[6] K. Yamaura, Y. Shirako, H. Kojitani, M. Arai, D. P. Young, M. Akaogi, M. Nakashima, T. Katsumata, Y. Inaguma, and E. Takayama-Muromachi, Synthesis and magnetic and charge-transport properties of the correlated 4*d* post-perovskite $CaRhO_3$, J. Am. Chem. Soc. **131**, 2722 (2009).

[7] K. Yamaura and E. Takayama-Muromachi, Enhanced paramagnetism of the 4*d* itinerant electrons in the rhodium oxide perovskite $SrRhO_3$, Phys. Rev. B **64**, 224424 (2001).

[8] J. Nichols, S. F. Yuk, C. Sohn, H. Jeen, J. W. Freeland, V. R. Cooper, and H. N. Lee, Electronic and magnetic properties of epitaxial $SrRhO_3$ films, Phys. Rev. B **95**, 245121 (2017).

[9] J. Zhou, Q.-F. Liang, H. Weng, Y. B. Chen, S.-H. Yao, Y.-F. Chen, J. Dong, and G.-Y. Guo, Predicted Quantum Topological HAll Effect and Noncoplanar Antiferromagnetism in $K_{0.5}RhO_2$, Phys. Rev. Lett. **116**, 256601 (2016).

[10] L. T. Nguyen, D. B. Straus, Q. Zhang, and R. J. Cava, Widely spaced planes of magnetic dimers in the $Ba_6Y_2Rh_2Ti_2O_{17-\delta}$ hexagonal perovskite, Phys. Rev. Mater. **5**, 034419 (2021).

[11] J. Terzic, J. C. Wang, F. Ye, W. H. Song, S. J. Yuan, S. Aswartham, L. E. DeLong, S. V. Streltsov, D. I. Khomskii, and G. Cao, Coexisting charge and magnetic orders in the dimer-chain iridate $Ba_5AlIr_2O_{11}$, Phys. Rev. B **91**, 235147 (2015).

[12] S. V. Streltsov, G. Cao, and D. I. Khomskii, Suppression of magnetism in $Ba_5AlIr_2O_{11}$: Interplay of Hund's coupling, molecular orbitals, and spin-orbit interaction, Phys. Rev. B **96**, 014434 (2017).

[13] L. T. Nguyen and R. J. Cava, Hexagonal perovskites as quantum materials, Chem. Rev. **121**, 2935 (2021).

[14] E. Şaşıoğlu, E. Sasioglu, C. Friedrich, and S. Blugel, Effective coulomb interaction in transition metals from constrained random-phase approximation, Phys. Rev. B **83**, 121101(R) (2011).

[15] S. V. Streltsov and D. I. Khomskii, Unconventional magnetism as a consequence of the charge disproportionation and the molecular orbital formation in $Ba_4Ru_3O_{10}$, Phys. Rev. B **86**, 064429 (2012).

[16] S. A. J. Kimber, I. I. Mazin, J. Shen, H. O. Jeschke, S. V. Streltsov, D. N. Argyriou, R. Valentí, and D. I. Khomskii, Valence bond liquid phase in the honeycomb lattice material Li_2RuO_3, Phys. Rev. B **89**, 081408(R) (2014).

[17] S. V. Streltsov and D. I. Khomskii, Covalent bonds against magnetism in transition metal compounds, Proc. Natl. Acad. Sci. USA **113**, 10491 (2016).

[18] P. Blaha, K. Schwarz, F. Tran, R. Laskowski, G. K. H. Madsen, and L. D. Marks, WIEN2k: An APW + lo program for calculating the properties of solids, J. Chem. Phys. **152**, 074101 (2020).

[19] B. J. Kim, H. Jin, S. J. Moon, J.-Y. Kim, B.-G. Park, C. S. Leem, J. Yu, T. W. Noh, C. Kim, S.-J. Oh, J.-H. Park, V. Durairaj, G. Cao, and E. Rotenberg, Novel $J_{\text{eff}} = 1/2$Mott State Induced by Relativistic Spin-Orbit Coupling in Sr_2IrO_4, Phys. Rev. Lett. **101**, 076402 (2008).

[20] B. Kim, H. Ohsumi, T. Komesu, S. Sakai, T. Morita, H. Takagi, and T.-h. Arima, Phase-sensitive observation of a spin-orbital Mott state in Sr_2IrO_4, Science **323**, 1329 (2009).

[21] X. Wan, A. M. Turner, A. Vishwanath, and S. Y. Savrasov, Topological semimetal and fermi-arc surface states in the electronic structure of pyrochlore iridates, Phys. Rev. B **83**, 205101 (2011).

[22] T. Mizokawa, L. H. Tjeng, G. A. Sawatzky, G. Ghiringhelli, O. Tjernberg, N. B. Brookes, H. Fukazawa, S. Nakatsuji, and Y. Maeno, Spin-Orbit Coupling in the Mott Insulator Ca_2RuO_4, Phys. Rev. Lett. **87**, 077202 (2001).

[23] H. Jin, H. Jeong, T. Ozaki, and J. Yu, Anisotropic exchange interactions of spin-orbit-integrated states in Sr_2IrO_4, Phys. Rev. B **80**, 075112 (2009).

[24] A. E. Taylor, R. Morrow, R. S. Fishman, S. Calder, A. I. Kolesnikov, M. D. Lumsden, P. M. Woodward, and A. D. Christianson, Spin-orbit coupling controlled ground state in Sr_2ScOsO_6, Phys. Rev. B **93**, 220408(R) (2016).

[25] V. I. Anisimov, F. Aryasetiawan, and A. I. Lichtenstein, First-principles calculations of the electronic structure and spectra of strongly correlated systems: the LDA + U method, J. Phys.: Condens. Matter **9**, 767 (1997).

[26] L. Xu, R. Yadav, V. Yushankhai, L. Siurakshina, J. van den Brink, and L. Hozoi, Superexchange interactions between spin-orbit-coupled $J \approx 1/2$ ions in oxides with face-sharing ligand octahedra, Phys. Rev. B **99**, 115119 (2019).

[27] K. I. Kugel, D. I. Khomskii, A. O. Sboychakov, and S. V. Streltsov, Spin-orbital interaction for face-sharing octahedra: Realization of a highly symmetric SU(4) model, Phys. Rev. B **91**, 155125 (2015).

[28] H. Singh, Determination of thermal expansion of germanium, rhodium and iridium by X-rays, Acta Crystallogr., Sect. A **24**, 469 (1968).

[29] L. Vaugier, H. Jiang, and S. Biermann, Hubbard U and Hund exchange J in transition metal oxides: Screening versus localization trends from constrained random phase approximation, Phys. Rev. B **86**, 165105 (2012).

[30] G. Cao and P. Schlottmann, The challenge of spin–orbit-tuned ground states in iridates: A key issues review, Rep. Prog. Phys. **81**, 042502 (2018).

[31] J. Hu and R. Wu, Giant magnetic anisotropy of transition-metal dimers on defected graphene, Nano Lett. **14**, 1853 (2014).

[32] T. O. Strandberg, C. M. Canali, and A. H. MacDonald, Transition-metal dimers and physical limits on magnetic anisotropy, Nat. Mater. **6**, 648 (2007).

[33] D. Dai, H. Xiang, and M.-H. Whangbo, Effects of spin-orbit coupling on magnetic properties of discrete and extended magnetic systems, J. Comput. Chem. **29**, 2187 (2008).

[34] D. Wang, F. Tang, Y. Du, and X. Wan, First-principles study of the giant magnetic anisotropy energy in bulk Na_4IrO_4, Phys. Rev. B **96**, 205159 (2017).